Nanoscale

PAPER

View Article Online
View Journal | View Issue

Cite this: *Nanoscale*, 2015, **7**, 9627

Electrocatalytic activity of alkyne-functionalized AgAu alloy nanoparticles for oxygen reduction in alkaline media†

Peiguang Hu, Yang Song, Limei Chen and Shaowei Chen*

Received 3rd March 2015,
Accepted 20th April 2015

DOI: 10.1039/c5nr01376c

www.rsc.org/nanoscale

1-Dodecyne-functionalized AgAu alloy nanoparticles were synthesized by chemical reduction of metal salt precursors at varied initial feed ratios. Transmission electron microscopic measurements showed that the nanoparticles were all rather well dispersed with the average core diameter in the narrow range of 3 to 5 nm. X-ray photoelectron spectroscopic studies confirmed the formation of AgAu alloy nanoparticles with the gold concentration ranging from approximately 25 at% to 55 at%. Consistent results were obtained in UV-vis spectroscopic measurements where the nanoparticle surface plasmon resonance red-shifted almost linearly with increasing gold concentrations. The self-assembly of 1-dodecyne ligands on the nanoparticle surface was manifested in infrared spectroscopic measurements. Importantly, the resulting nanoparticles exhibited apparent electrocatalytic activity for oxygen reduction in alkaline media, and the performance was found to show a volcano variation in the Au content in the alloy nanoparticles, with the best performance observed for the samples with *ca.* 35.5 at% Au. The enhanced catalytic activity, as compared to pure Ag nanoparticles or even commercial Pt/C catalysts, was accounted for by the unique metal–ligand interfacial bonding interactions as well as alloying effects that increased metal–oxygen affinity.

Introduction

Low-temperature fuel cell technology has been attracting considerable interest as a means of directly converting chemical energy into electrical energy because of the attractive efficiency and environmental benefits.[1,2] The types of fuel cells under active development include alkaline fuel cells (AFC), polymer electrolyte membrane fuel cells (PEMFC), and alkaline polymer electrolyte fuel cells (APEFC).[1,3] In these systems, because of the sluggish kinetics of the oxygen reduction reaction (ORR) at the cathode, $O_2 + 2H_2O + 4e^- \rightarrow 4OH^-$, a large amount of platinum is typically required to catalyze the reaction so that a sufficiently high current density can be generated for practical applications.[4] Such dependence on Pt catalysts has significantly hindered the widespread application of fuel cells due to the high costs and limited reserves of Pt.[4] Therefore, numerous efforts have been devoted to the improvement of Pt efficiency and/or to the development of Pt-free effective alternative catalysts.[5–8] In recent years, non-Pt catalysts, such as carbon nanomaterials,[9,10] metal oxides,[11,12] and non-Pt-group metals,[13–15] have been reported to exhibit considerable mass-specific activities. However, carbon nanomaterials and metal oxides in general suffer from low volume-specific activity and insufficient electronic conductivity, respectively. Non-Pt metals or metal alloys might be a promising alternative because of their high electronic conductivity and abundant catalytic sites to fulfil the requirements for fuel cell catalysis,[13,16,17] especially with the significant progress in the study of alkaline polymer electrolytes used in APEFC,[18,19] which provide a low-corrosion environment to mitigate the instability of non-Pt metal catalysts in acidic electrolytes commonly used in PEMFC.

Among these, silver has been gaining increasing attention as a viable candidate for non-Pt catalyst materials for ORR in alkaline media since the early stage of AFC.[20–22] Compared with other non-Pt catalysts, such as Pd,[23,24] Au,[25,26] Ni,[27,28] and Co,[27,28] silver is relatively inexpensive and displays high catalytic activity where ORR proceeds *via* the 4-electron reduction route.[21,22] However, the overall catalytic activity of Ag for ORR remains inferior to that of Pt, as manifested by a more negative onset potential, lower kinetic current density, and smaller electron-transfer number. Apparently, further improvement of the ORR activity is necessary in order for silver to be competitive and viable in ORR electrocatalysis. This is the primary motivation of the present study.

Department of Chemistry and Biochemistry, University of California, 1156 High Street, Santa Cruz, California 95064, USA. E-mail: Shaowei@ucsc.edu

† Electronic supplementary information (ESI) available: Effective electrochemical surface areas by oxygen adsorption and Koutecky-Levich plots. See DOI: 10.1039/c5nr01376c

Note that a number of strategies have been proposed and explored to improve the electrocatalytic performance of metal catalysts for ORR, including manipulation of elemental composition,[29–31] size,[31–33] morphology,[31,34–36] and surface atomic arrangement.[31,37,38] Whereas the enhancement mechanism has not been fully understood, modification of the d-band centers and formation of lattice geometrical strains have been suggested as two leading factors that may impact the binding of oxygen and reaction intermediates on the metal surfaces and hence the eventual ORR performance. Of these, alloying with a second metal is an effective route to the enhancement of the ORR performance by combining the effects of elemental composition and surface structures of the metal catalysts.[29,39,40] Remarkably, whereas the ORR catalytic performance of gold alone is even lower, AgAu alloyed catalysts have been found to display a significantly improved performance as a result of increasing metal–oxygen affinity.[3,41] For instance, by coating Ag onto Au electrode surfaces, the ORR activity in 0.1 M KOH was found to increase by half an order of magnitude.[3] In another study, by incorporating only *ca.* 5% of gold onto Ag nanoparticles by galvanic exchange reactions, the resulting nanoparticles were over seven times more active than the original silver nanoparticles in ORR.[41]

It should be noted that in these prior studies, the composition of the AgAu bimetallic alloy catalysts has remained unoptimized for ORR. Herein, 1-dodecyne functionalized AgAu alloy nanoparticles were prepared by chemical reduction of metal salt precursors at different initial feed ratios and used as a model system to examine the ORR electrocatalytic activity, using pure Ag nanoparticles as the comparative example.[41,42] This is partly motivated by some of our previous studies where alkynes served as effective capping ligands for nanoparticle stabilization and functionalization and the resulting nanoparticles exhibited apparent electrocatalytic activity, as compared to those capped with alkanethiolates, thanks to the unique metal–ligand interfacial bonding interactions.[43,44] The results indicated that the sample with *ca.* 35.5 at% Au exhibited the best ORR catalytic activity among the series, most probably as a result of the optimized metal–oxygen affinity.

Experimental section

Chemicals

Silver nitrate ($AgNO_3$, Fisher Scientific), hydrogen tetrachloroauric acid ($HAuCl_4$, Acros), sodium borohydride ($NaBH_4$, ≥98%, Acros), tetra-*n*-octylammonium bromide (TOABr, 98%, Acros), 1-oleylamine (>40%, TCI), and 1-dodecyne (98%, Acros) were all used as received without any further purification. Solvents were purchased at the highest purity available from typical commercial sources and also used as received. Water was deionized with a Barnstead Nanopure water system (18.3 MΩ cm).

Synthesis of AgAu alloy nanoparticles

Experimentally, $AgNO_3$ and $HAuCl_4$ (2 mmol in total at six different feed ratios, denoted as #1 to #6 with decreasing Au contents) were dissolved in 5 mL of water. The solution was mixed with 5 mL of a toluene solution of TOABr (0.6 mmol) under vigorous stirring for 1 h. The organic phase was then collected, into which was added 400 μL of 1-oleyamine. After magnetic stirring for 1 h, 1 mL of a freshly prepared $NaBH_4$ solution (80 mg mL^{-1}) in water was added into the solution where the color was found to turn dark red immediately, signifying the formation of nanoparticles. The reaction mixture was stirred for 4 h before the organic phase was collected and washed five times with methanol to remove the phase transfer catalysts, excessive reagents, and reaction byproducts. The collected nanoparticles were then dissolved in CH_2Cl_2 along with 0.6 mmol of 1-dodecyne. The mixed solutions were stirred overnight and washed with methanol five times to remove free ligands.

Characterization

The morphology and size of the nanoparticles were characterized by transmission electron microscopic studies (TEM, Philips CM300 at 300 kV). Experimentally, a dilute solution of the nanoparticles (<1 mg mL^{-1} in CH_2Cl_2) was prepared and dropcasted onto a TEM grid. At least 200 nanoparticles were measured to obtain a size histogram. UV-vis spectra were collected with a Unicam ATI UV4 spectrometer using a 1 cm quartz cuvette. FTIR measurements were carried out with a Perkin-Elmer FTIR spectrometer (Spectrum One, spectral resolution 4 cm^{-1}), where the samples were prepared by casting the particle solutions onto a NaCl disk. X-ray photoelectron spectra (XPS) were recorded with a PHI 5400/XPS instrument equipped with an Al Kα source operated at 350 W and 10^{-9} Torr. Silicon wafers were sputtered by using argon ions to remove carbon from the background and used as substrates with the binding energy of Si 2p electrons as the reference.

Electrochemistry

The electrochemical setup consisted of a CHI710 electrochemical workstation with a Pt counter electrode and a Ag/AgCl reference electrode at room temperature. The working electrode was a rotating ring-disk electrode (RRDE, AFE7R9GCAU from Pine Instrument Co.) with a glassy carbon disk (GC, diameter 5.61 mm) and a gold ring. The collection efficiency (N) was determined to be 40% by RRDE measurements in 5 mM $K_4Fe(CN)_6$ + 0.1 M KNO_3.[45] The RRDE electrode was prepared according to a procedure proposed by Gloaguen *et al.*,[46] which has been used extensively in ORR studies.[47–52] In a typical experiment, 250 μg of the AgAu nanoparticles was mixed with 1 mg of XC-72 carbon black (metal : carbon mass ratio = 1 : 4) in 250 mL of toluene with 2.5 μL of a Nafion® 117 solution (5 wt%) and dispersed under sonication. A measured volume (*ca.* 6 μL) of this catalyst ink was then transferred *via* a Hamilton microliter syringe onto the freshly polished glassy carbon disk. The solvent was evaporated at room temperature yielding a catalytic loading of 30 μg with *ca.* 6 μg of nanoparticles (20 wt%).

Results and discussion

The size and morphology of the AgAu alloy nanoparticles were first characterized by TEM measurements, as shown in Fig. 1. It can be seen that the nanoparticles were all dispersed very well without significant aggregation, indicating effective protection of the nanoparticles by using the 1-dodecyne ligands. Statistical analysis based on over 200 nanoparticles showed that the average core diameter of the AgAu alloy nanoparticles was rather consistent at around 4.0 nm, except for sample #6 which is somewhat larger: (A, #1) 3.85 ± 0.64 nm, (B, #2) 3.97 ± 0.94 nm, (C, #3) 3.78 ± 0.95 nm, (D, #4) 3.68 ± 0.67 nm, (E, #5) 3.79 ± 0.84 nm, and (F, #6) 5.17 ± 1.14 nm, as depicted in the respective upper inset (and summarized in Table 1). Furthermore, the nanoparticles all exhibited well-defined crystalline lattice fringes, as highlighted in the lower insets, with an interlayer spacing of 0.235 nm that is consistent with the (111) planes of both fcc silver (PDF Card #4-783) and gold (PDF Card #4-784).

The elemental compositions of the AgAu alloy nanoparticles were then quantified by XPS measurements. Fig. 2 depicts the survey profiles for the (left panel) Ag 3d and (right panel) Au 4f electrons of the six nanoparticle samples. It can be seen that the binding energies of the Ag 3d electrons for all samples were rather consistent with a doublet centered at 367.9 and 373.9 eV, suggesting metallic silver in the nanoparticles.[53,54] Similar behaviors can be observed with the Au 4f electrons where the doublets were centered at 83.8 and 87.4 eV for all samples, in good agreement with Au(0).[55] In addition, based on the ratio of the integrated peak areas of the Ag 3d and Au 4f electrons, the atomic fractions of gold in the alloy nanoparticles were estimated to be (A, #1) 56.5%, (B, #2) 51.5%, (C, #3) 39.2%, (D, #4) 35.5%, (E, #5) 31.2%, and (F, #6) 26.7%, which is consistent with the results from UV-vis spectroscopic measurements (*vide infra*). The results are also summarized in Table 1.

Fig. 3 shows the UV-vis absorption spectra of the six AgAu alloy nanoparticles. It can be seen that all samples exhibited an exponential decay profile, arising from the so-called Mie scattering of nanosized metal nanoparticles, onto which is superimposed an apparent absorption peak that is the surface plasmon resonance (SPR) characteristic of the corresponding nanoparticles. It is known that pure gold and silver nanoparticles exhibit well-defined SPR in the visible region at around 520 nm and 400 nm, respectively.[56] For gold and silver alloy nanoparticles, the SPR peak is typically found between these two wavelength positions, varying with the elemental compositions of the nanoparticles.[57] In fact, from the inset of Fig. 3, it can be seen that the SPR peak positions exhibited an almost linear red-shift with increasing gold contents in the alloy nanoparticles: 482 nm (sample #1, black curve), 480 nm (sample #2, red curve), 464 nm (sample #3, green curve), 436 nm (sample #4, yellow curve), 434 nm (sample #5, blue curve), and 421 nm (sample #6, pink curve). Furthermore, the appearance of a single absorption peak suggests that the AgAu alloy nanoparticles rather than a simple mixture of gold and silver monometallic nanoparticles were formed. Note that Link and coworkers have reported similar observations, in which the surface plasmon band position of gold-silver alloy nanoparticles was found to shift linearly with the atomic contents.[58]

The successful incorporation of 1-dodecyne ligands onto the surface of AgAu alloy nanoparticles was manifested in FTIR measurements. Fig. 4 shows the FTIR spectra of the six AgAu alloy nanoparticle samples (solid curves). The most significant observation is the disappearance of the ≡C–H vibrational stretch at 3314 cm^{-1} which is well-defined with monomeric alkynes (dashed curve), suggesting the ready cleavage of the ≡C–H bonds upon the self-assembly of the ligands onto the AgAu alloy nanoparticle surface. In addition, the vanished ≡C–H vibrational stretch also indicates that the nanoparticles were free of excessive monomeric ligands. Furthermore, the C≡C stretch, which appeared at 2119 cm^{-1} for the monomeric ligands (dashed curve), was found to red-shift and split into two bands at around 1990 cm^{-1} and 2060 cm^{-1}. This may be ascribed to intraparticle charge delocalization as a result of the formation of conjugated M(Ag/Au)–C≡ interfacial bonds such that the particle-bound acetylene moieties behaved analogously to diacetylene derivatives (C≡C–C≡C) (additional contributions may arise from the formation of M(Ag/Au)–H bonds on the nanoparticle surface[59,60]). Similar behaviors have also been observed previously with nanoparticles functionalized with other acetylene derivatives.[44,61,62]

The electrocatalytic activity in oxygen reduction of the six samples prepared above was then examined and compared by electrochemical measurements. Note that before oxygen reduction reaction measurements, the catalysts-modified electrodes were subjected to an electrochemical activation treatment by rapid potential cycling (at 500 mV s^{-1}) between 0 and +1.2 V (*vs.* RHE) in a nitrogen-saturated 0.1 M NaOH solution until a steady voltammogram was obtained. The adsorption of oxygen was used for the quantitative assessments of the effective electrochemical surface area (ECSA, Fig. S1†) and the results are summarized in Table 1. It can be seen that ECSA exhibited a roughly monotonic decrease with decreasing gold (increasing silver) contents in the AgAu nanoparticles, probably because of the somewhat stronger bonding interactions of alkynes with Ag than with Au,[41,42] which led to fewer ligands being removed during the electrochemical activation process at higher Ag concentrations. In fact, in comparison with the geometrical surface area of the nanoparticles (assuming a spherical shape), the fraction of the nanoparticle surface that was electrochemically accessible can be estimated to be (#1) 41.5%, (#2) 41.2%, (#3) 25.9%, (#4) 33.4%, (#5) 21.6%, and (#6) 23.1%. This also implied only partial removal of the alkyne capping ligands from the nanoparticle surface. Similar behaviors have been observed previously.[45]

Fig. 5 depicts the RRDE voltammograms of a glassy-carbon disk electrode modified with a calculated amount of each sample in an oxygen-saturated 0.1 M NaOH solution at varied rotation rates (from 100 to 2500 rpm). It can be seen that for all samples, apparent cathodic currents at the disk electrode

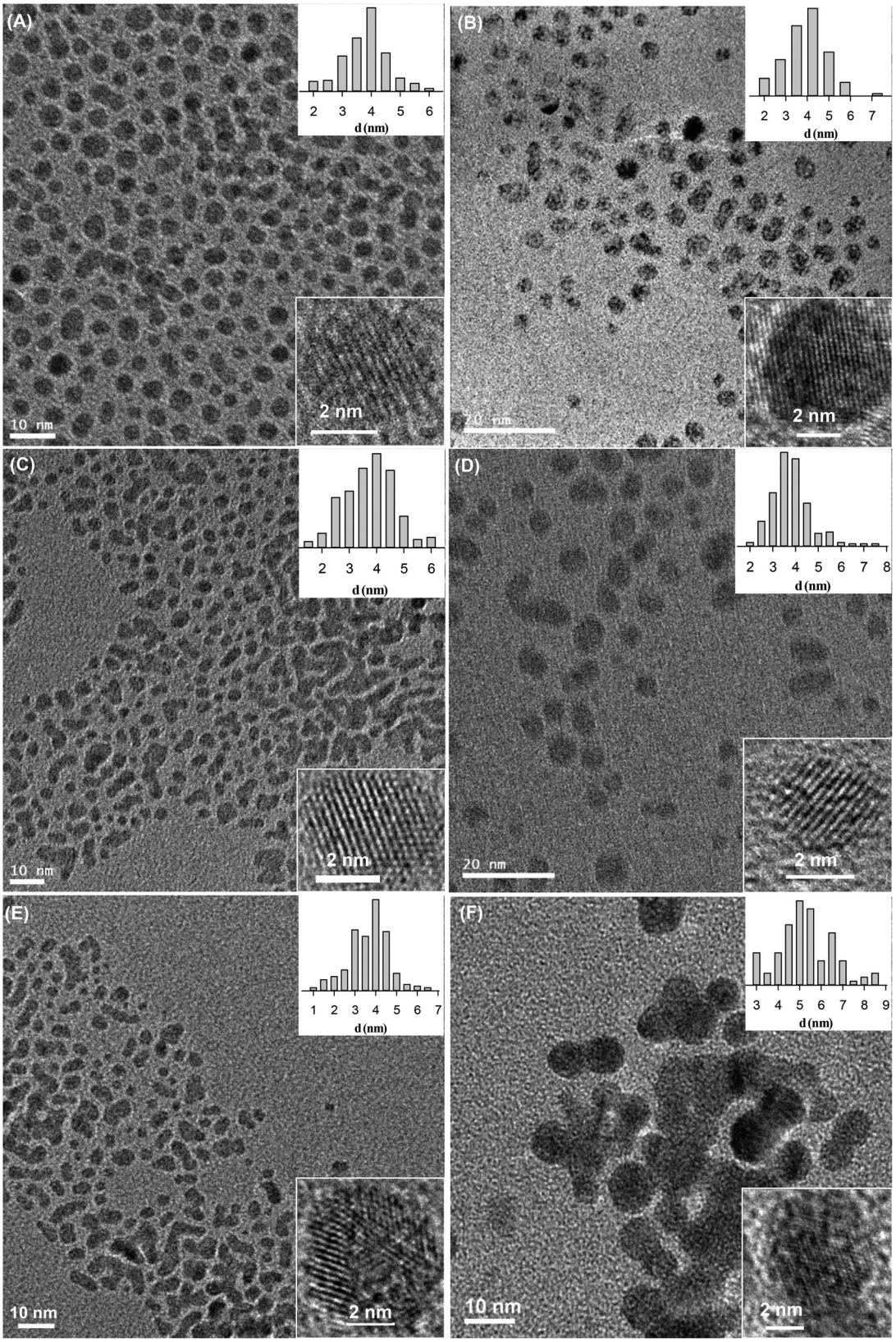

Fig. 1 Representative TEM micrographs of AgAu nanoparticles at varied atomic compositions: (A) #1, (B) #2, (C) #3, (D) #4, and (E) #5, and (F) #6. Lower insets are the corresponding high-resolution images and upper insets the core size histograms.

Table 1 Summary of the average core diameter (d, nm), gold atomic concentration (at%), electrochemical surface area (ECSA, $m^2\ g^{-1}$), onset potential (E_{onset}, V *vs.* RHE), specific activity (J_s, A m^{-2}), mass activity (J_m, A g^{-1}) and Tafel slopes in ORR of AgAu nanoparticles

AgAu	#1	#2	#3	#4	#5	#6
d (nm)	3.85 ± 0.64	3.97 ± 0.94	3.78 ± 0.95	3.68 ± 0.67	3.79 ± 0.84	5.17 ± 1.14
Au at%	56.5	51.5	39.2	35.5	31.5	26.7
ECSA ($m^2\ g^{-1}$)	41.8	41.4	29.5	40.0	25.8	20.9
E_{onset} (V)	+0.90	+0.90	+0.90	+0.92	+0.91	+0.89
J_s (A m^{-2}, at +0.85 V)	1.80	0.81	1.47	2.39	1.75	1.83
J_m (A g^{-1}, at +0.85 V)	75.2	33.5	43.4	95.6	45.2	38.2
Tafel slope (mV dec^{-1})						
J_s < 2.5 A m^{-2}	58.4	66.6	63.1	62.4	84.8	89.2
J_s > 2.5 A m^{-2}	108.6	113.1	115.9	109.4	109.5	131.6

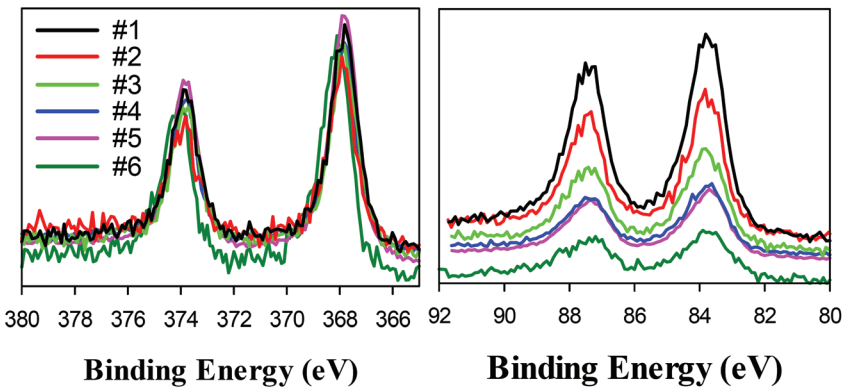

Fig. 2 XPS spectra of the (left panel) Ag3d and (right panel) Au 4f electrons of the six AgAu alloy nanoparticles.

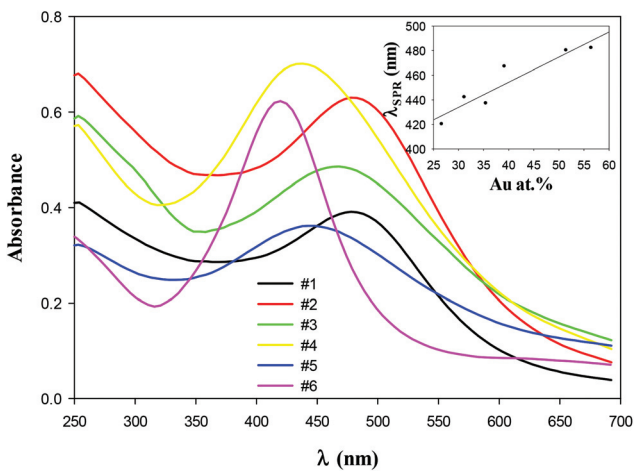

Fig. 3 UV-vis absorption spectra of the six AgAu alloy nanoparticles in CH_2Cl_2. The inset shows the variation in the corresponding SPR positions with gold contents in the nanoparticles. Symbols are experimental data and line is the linear regression.

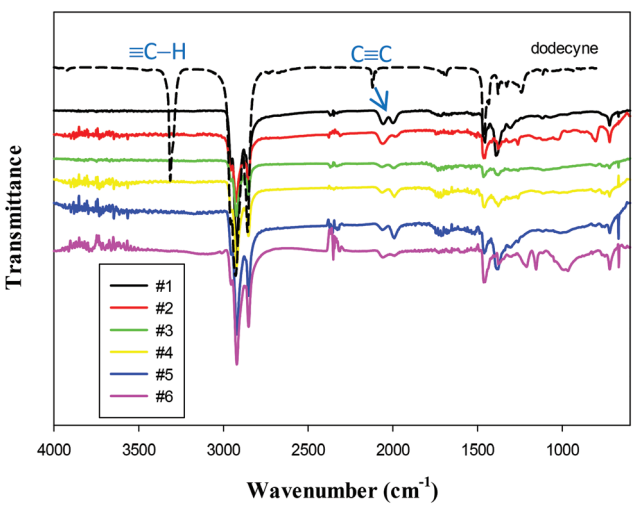

Fig. 4 FTIR spectra of AgAu nanoparticles at varied atomic compositions (solid curves). The spectrum for the 1-dodecyne monomers is also included as the dashed curve.

started to emerge at around +0.9 V (*vs.* RHE) and the currents reached a plateau at sufficiently negative potentials (around +0.6 V *vs.* RHE), which suggests effective electrochemical activity in oxygen reduction, despite (partial) capping of the metal cores by the organic ligands; and the voltammetric currents increased with increasing electrode rotation rates. Yet, the performance can be seen to vary somewhat with the elemental compositions of the nanoparticle catalysts. For

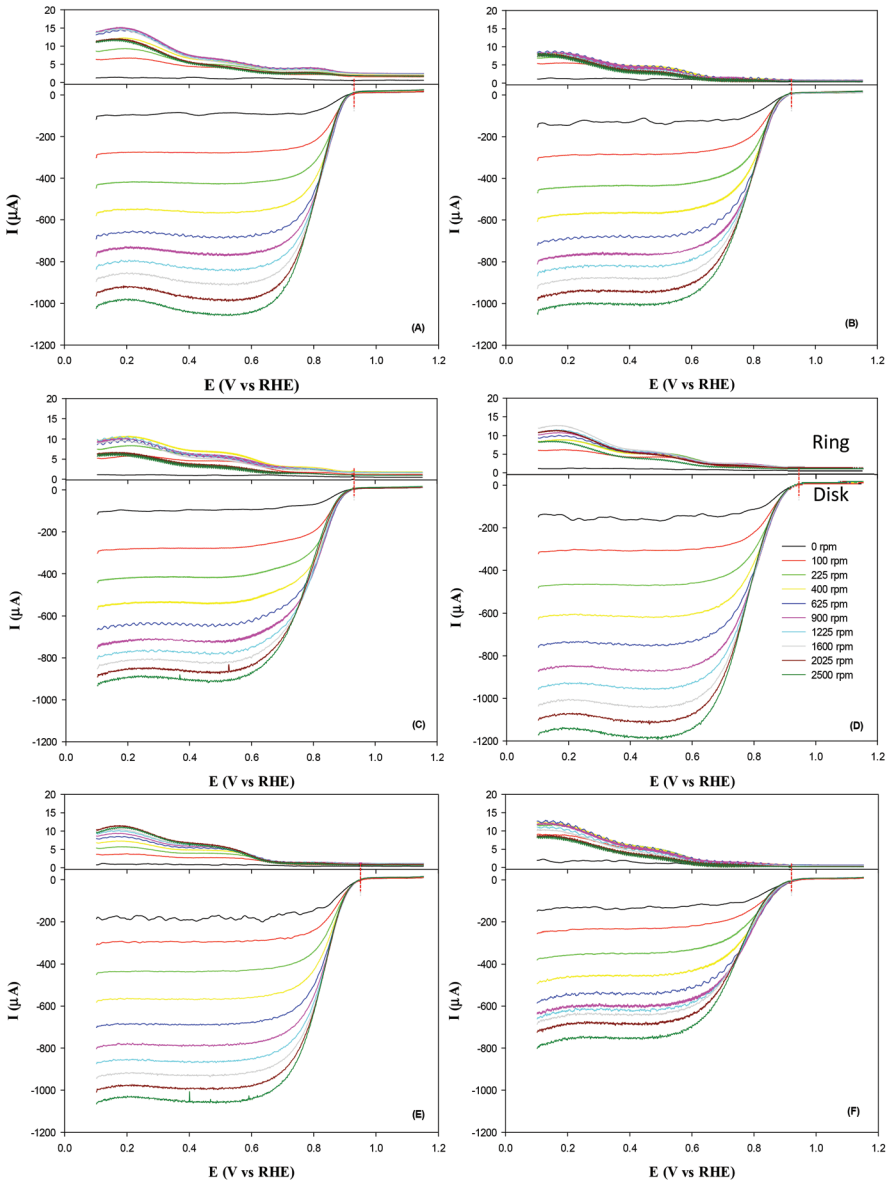

Fig. 5 RRDE voltammograms of a glassy carbon electron modified with the six AgAu nanoparticles in oxygen-saturated 0.1 M NaOH at varied rotation rates (specified in figure legends). Red vertical bars indicate the onset potentials. The loading of AgAu nanoparticle catalysts was all 6 μg. Disk potential ramp was 10 mV s^{-1} and the ring potential was set to +1.5 V.

instance, at any given rotation rate, the limiting currents appear to be maximal with sample (D). In fact, at the same catalyst loadings, the limiting currents at +0.50 V at 1600 rpm are (A, #1) 912 μA, (B, #2) 880 μA, (C, #3) 823 μA, (D, #4) 1040 μA, (E, #5) 928 μA, and (F, #6) 634 μA. A similar trend can be seen with the onset potentials (Table 1): (A, #1) +0.90 V, (B, #2) 0.90 V, (C, #3) +0.90 V, (D, #4) +0.92 V, (E, #5) +0.91 V, and (F, #6) +0.89 V. Note that in a previous study with alkanethiolate-passivated silver nanoparticles of similar size, the onset potential was found to be markedly more negative at around +0.80 V.[41] These observations suggest that sample (D) (with 35.5 at% of Au) stood out as the best catalyst in the series, which is rather comparable to leading commercial Pt/C catalysts.[63]

In addition, the amounts of hydrogen peroxide generated during the oxygen reduction reaction were monitored by collection experiments at the ring electrode which was set to a potential of +1.5 V (*vs.* RHE). It is clear from Fig. 5 that the ring currents were about two orders of magnitude smaller than those on disk electrodes at all rotation rates for all samples. In fact, the number of electrons transferred (n) during the oxygen reduction reaction can be estimated by $n = 4I_D/(I_D + I_R/N)$, where I_D and I_R are the disk and ring currents, respectively.[45] By using disk and ring currents generated at 1600 rpm as an example, n values were calculated for all AgAu nanoparticles, as shown in Fig. 6. Notably, all the six samples exhibited a remarkable ORR performance, with the n values in

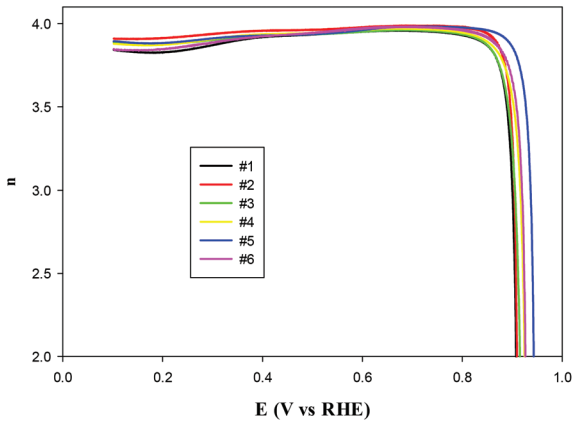

Fig. 6 Variation in the number of electrons transferred (*n*) in ORR at AgAu nanoparticles with electrode potentials. Data were calculated from the RRDE voltammograms at 1600 RPM in Fig. 5.

the narrow range of 3.8 to 4.0 within the wide potential range of +0.85 to +0.10 V, suggesting that oxygen primarily underwent four-electron reduction to hydroxide (OH^-) with minimal amounts of peroxide byproducts. In contrast, in the previous study with hexanethiolate-passivated silver nanoparticles, the *n* value at similar electrode potentials was much lower at only *ca.* 2.5, which was improved to a little over 3.0 when ~5 at% Au was incorporated onto the nanoparticles by interfacial engineering.[41] Taken together, these results suggest that alloying of silver nanoparticles with gold is effective in improving the ORR activity which may be optimized at a controlled gold concentration.

In order to quantitatively compare the intrinsic catalytic activity, the electron-transfer kinetics was further analyzed by the Koutecky–Levich method, as shown in Fig. S2.† As the disk voltammetric current (I_D) may include both kinetic (I_k) and diffusion-controlled (I_d) contributions, the Koutecky–Levich equation is expressed as follows:

$$\frac{1}{I_D} = \frac{1}{I_k} + \frac{1}{I_d} = \frac{1}{I_k} + \frac{1}{B\omega^{1/2}} \quad (1a)$$

$$B = 0.62nFAC_O{D_O}^{2/3}\nu^{-1/6} \quad (1b)$$

$$I_k = nAFkC_O \quad (1c)$$

where ω is the electrode rotation rate, n is the electron-transfer number, F is the Faraday constant (96 485 C mol^{-1}), A is the geometric surface area of the electrode, C_O is the oxygen concentration in O_2-saturated solutions (1.26×10^{-6} mol cm^{-3}),[64] D_O is the diffusion coefficient of O_2 in 0.1 M NaOH aqueous solution (1.93×10^{-5} cm^2 s^{-1}),[65] ν is the kinematic viscosity of the solution (1.09×10^{-2} cm^2 s^{-1}),[66] k is the electron-transfer rate constant. In fact, all six sample catalysts show good linearity of the Koutecky–Levich plots (I_D^{-1} *vs.* $\omega^{-1/2}$) within the potential range of +0.75 V to +0.85 V, where contributions from the kinetic component were significant, and the slopes were rather consistent for each nanoparticle suggesting consistent electron transfer kinetics within the electrode potential range. This observation is usually taken as a strong indication of a first-order reaction with respect to dissolved oxygen.

In addition, the kinetic currents might be quantitatively estimated from the *y*-axis intercepts of the linear regression of the Koutecky–Levich plots, as depicted in the Tafel plot of Fig. 7. It can be seen that for all nanoparticle catalysts, the area-specific kinetic current density (J_s, I_k normalized by the respective ECSA in Table 1 and Fig. S1†) increased as the potential became more negative. Yet, the specific activity varied rather sensitively with the nanoparticle compositions. For instance, at +0.85 V, J_k increases in the order of (#2) 0.81 A m^{-2} < (#3) 1.47 A m^{-2} < (#5) 1.75 A m^{-2} < (#1) 1.80 A m^{-2} < (#6) 1.83 A m^{-2} < (#4) 2.39 A m^{-2}. A similar trend can be seen with the mass-specific activity (J_m, I_k normalized by the nanoparticle mass loading): (#2) 33.5 A g^{-1} < (#6) 38.2 A g^{-1} < (#3) 43.4 A g^{-1} < (#5) 45.2 A g^{-1} < (#1) 75.2 A g^{-1} < (#4) 95.6 A g^{-1}. These data are also listed in Table 1. The comparison can be better manifested in the inset of Fig. 7 where the specific activity exhibited a volcano-shaped variation in the gold contents in the alloy nanoparticles and reached the maximum with sample #4, suggesting that the optimal concentration of Au was about 35.5 at% for ORR. Note that no apparent kinetic current and hence ORR catalytic activity was observed for polycrystalline silver electrodes, monometallic Ag nanoparticles or AgAu bimetallic Janus nanoparticles (*ca.* 5 at% of Au) at the same electrode potential.[41,67]

Furthermore, the Tafel plots of the six nanoparticle catalysts display two linear segments of different slopes (Table 1). One should note that for the oxygen reduction reaction, the Tafel slopes are typically found at 60 mV dec^{-1} or 120 mV dec^{-1}, where the former corresponds to a pseudo two-electron reaction as the rate determining step, and the latter one suggests that the rate determining step is presumed to be a first-electron reduction of oxygen, implying that the subsequent

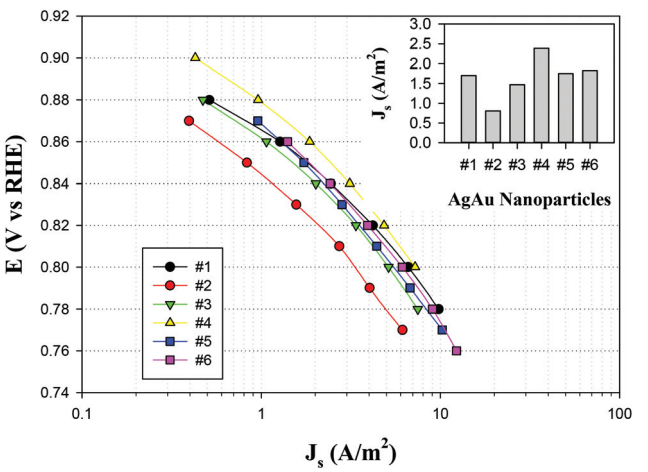

Fig. 7 Tafel plot of the AgAu nanoparticles in oxygen reduction. Symbols are experimental data extracted from the *y*-axis intercepts of the corresponding Koutecky–Levich plots and lines are for eye-guiding only. The inset shows the comparison of the kinetic current density at +0.85 V among the six AgAu nanoparticle samples.

reduction and O–O bond breaking steps are facile.[68] In the present study, at the kinetic current densities lower than 2.5 A m^{-2} (low overpotential region), linear regressions show that the slopes are all close to 60 mV dec^{-1} except for samples #5 and #6 where the slopes are close to 90 mV dec^{-1}; whereas at kinetic current densities above 2.5 A m^{-2} (high overpotential region), the corresponding slopes were all around 120 mV dec^{-1}. These observations suggest a similar oxygen reduction mechanism for the six AgAu alloy nanoparticles. That is, in the low overpotential region, the reaction rate was mainly controlled by the pseudo two-electron reduction reaction (possibly involving the breaking of the O–O bonds), whereas at high overpotentials the rate determining step was likely the first-electron reduction of oxygen. Such Tafel behaviors have been also observed and reported previously for Pt or Pd catalysts,[69] suggesting that the catalytic mechanism of ORR on AgAu resembles that on Pt or Pd, which involves O–O bond breaking and adsorption of oxygenate intermediates, but is distinctly different from that on pure Ag or Au catalysts, where it could be kinetically favorable for outer-sphere electron transfers.[70]

It is most likely that the improved performance (with onset potentials up to +0.92 V and a remarkable kinetic current density) of AgAu alloy nanoparticles over Ag or Au nanoparticles alone is due to the enhanced surface oxygen absorption. It has been shown by both theoretical calculations and experimental studies that the adsorption energies (AE) of oxygen could be manipulated by metal alloying, where the effect on the AE of oxygen is not linearly dependent on the original AE.[3,71] In fact, it has been reported by Wang *et al.* that more O_2^- species were found on the AgAu alloy surface than on pure Ag or Au surfaces, and the amount of O_2^- species varied with different Ag/Au ratios.[72] Therefore, in the present study, it is most likely that the marked enhancement of the ORR performance was due to improved surface oxygen affinity by alloying Ag and Au, leading to a positive shift of the equilibrium potential for the first electron transfer reaction and hence a reduced overpotential and positive shift of the onset potential.[70] Moreover, enhanced absorption of oxygen also facilitates the breaking of the O–O bond, resulting in an increase of kinetic current densities. Nevertheless, the increased surface affinity toward oxygen is at the expense of forming strongly bound O and OH species as a result of water oxidation.[73] If the O and OH species produced during ORR are strongly adsorbed onto the catalyst surface, further reduction of O_2 may be inhibited, since the activation energies for O and OH reduction have been found to be relatively high in the low overpotential region in which fuel cell cathodes would ideally be operated.[2] Thus, an optimal oxygen affinity is required to be strong enough to facilitate the first electron transfer to oxygen, but not too strong to inhibit the release of absorbed OH species. Results presented above show that AgAu alloy nanoparticles with approximately 35.5 at% gold display the optimal oxygen affinity, leading to the highest kinetic current density among the series.

As shown in Table 2, the electrocatalytic performance of the AgAu nanoparticles prepared above for ORR remained subpar as compared to that of state-of-the art commercial Pt/C catalysts that typically exhibit an onset potential more positive than +0.96 V, a specific activity (J_s) of ~2 A m^{-2} and a mass activity (J_m) of 160 A g^{-1} even at +0.90 V.[45] However, the ORR activity of the AgAu nanoparticles in the present study, especially sample #4 (n = 3.8 to 4.0 within the potential range of +0.10 V to +0.85 V, onset potential +0.92 V, J_s = 2.39 A m^{-2}, and J_m = 95.6 A g^{-1} at +0.85 V), was markedly better than, or at least comparable to, that of leading Ag-based electrocatalysts reported in the literature. For instance, Slanac *et al.* prepared AgPd alloy particles (dia. ~5 nm) by simultaneous reduction of Ag and Pd precursors and found that Ag_4Pd exhibited the best electrocatalytic activity (n = 3.7, onset potential +0.91 V, J_m = 598 A g^{-1} at the potential of +0.72 V) for ORR.[80] In another study, Ag_4Pd alloy particles were prepared by co-reduction of Ag and Pd salts and deposited on multiwalled carbon nanotube (MWCNT) surfaces, which exhibited an onset potential of +0.91 V for ORR, but with a low n number of only 2.25 and a low specific activity of only 0.22 A m^{-2}.[78] In contrast, Jiang *et al.* reported a rather high ORR activity with Pd@Ag/C hybrids (onset potential +0.93 V, J_s = 32 A m^{-2}, and J_m = 1000 A g^{-1} at +0.85 V). However, the Pd@Ag/C hybrids were synthesized by growing Pd onto the surface of carbon supported Ag nanoparticles, where the catalytic activity was most likely due to Pd on the surface whereas the Ag component was not even involved in the catalytic reaction.[79] In another study,

Table 2 Summary of ORR activity of leading Ag-based and Pt/C electrocatalysts for ORR in the literature

	J_s (A/m^2, at +0.85 V *vs.* RHE)	J_m (A/g, at +0.85 V *vs.* RHE)	n	E_{onset} (V *vs.* RHE)
AgAu Janus nanoparticles[41]			3.36	+0.80
Ag nanoparticles–MWCNTs[74]	~1 (+0.80 V)			+0.81
Ag nanoparticles (15 wt.%)-ECNF[75]			3.9	+0.88
Core–shell–shell Ag–Pt–Ag nanocubes[76]		~1.78	3.95	+0.90
Ag–MnO_x/VC[77]		<125 (+0.82 V)	3.5	+0.92
Ag_4Pd_1/MWCNTs[78]	~0.22		2.25	+0.91
Pd@Ag/C[79]	~32	1000		+0.93
Au@Ag[3]	~1.6			+0.92
Ag_4Pd[80]			3.7	+0.91
Ag nanosheets on Ti/TiO_2 electrode[81]		~0.063		+0.92
Pt/C[45]	2 (+0.90 V)	~160 (+0.90 V)	~4	+0.96

Tsai *et al.* prepared core–shell–shell Ag–Pt–Ag nanocubes by epitaxial growth. Despite the incorporation of Pt into the alloy structures, the ORR activity was rather modest with n = 3.95, onset potential +0.90 V, and J_m = 1.78 A g^{-1} at +0.85 V.[76]

Conclusions

In summary, 1-dodecyne-capped AgAu alloy nanoparticle samples were successfully prepared by chemical reduction of the metal salt precursors at varied initial feed ratios. TEM measurements showed that the resulting nanoparticles exhibited an average core size within the narrow range of 3 to 5 nm in diameter, and XPS measurements showed that the corresponding gold contents varied from about 25 at% to 55 at%. Consistent results were obtained in UV-vis absorption measurements, where an almost linear red-shift of the plasmon absorption peak positions was observed with increasing Au content. More importantly, electrochemical measurements showed that the alloy nanoparticles all exhibited apparent electrocatalytic activity for ORR, and the sample with 35.5 at% Au was found to display the best catalytic activity among the series, within the context of onset potential, number of electrons transferred and kinetic current density. Such a performance is likely due to the unique metal–ligand interfacial bonding interactions as well as enhanced metal–oxygen affinity from the alloying effects.

Acknowledgements

This work was supported in part by the National Science Foundation (CHE-1265635 and DMR-1409396). TEM and XPS work was carried out at the National Center for Electron Microscopy and Molecular Foundry, Lawrence Berkeley National Laboratory as part of a user project.

Notes and references

1 B. C. H. Steele and A. Heinzel, *Nature*, 2001, **414**, 345–352.
2 J. K. Norskov, J. Rossmeisl, A. Logadottir, L. Lindqvist, J. R. Kitchin, T. Bligaard and H. Jonsson, *J. Phys. Chem. B*, 2004, **108**, 17886–17892.
3 C. Yang, B. Huang, L. Xiao, Z. Ren, Z. Liu, J. Lu and L. Zhuang, *Chem. Commun.*, 2013, **49**, 11023–11025.
4 D. P. Tang, J. Pan, S. F. Lu, L. Zhuang and J. T. Lu, *Sci. China Chem.*, 2010, **53**, 357–364.
5 H. A. Gasteiger, S. S. Kocha, B. Sompalli and F. T. Wagner, *Appl. Catal., B*, 2005, **56**, 9–35.
6 T. Toda, H. Igarashi, H. Uchida and M. Watanabe, *J. Electrochem. Soc.*, 1999, **146**, 3750–3756.
7 Z. C. Liu, S. Koh, C. F. Yu and P. Strasser, *J. Electrochem. Soc.*, 2007, **154**, B1192–B1199.
8 V. R. Stamenkovic, B. S. Mun, M. Arenz, K. J. J. Mayrhofer, C. A. Lucas, G. F. Wang, P. N. Ross and N. M. Markovic, *Nat. Mater.*, 2007, **6**, 241–247.
9 K. P. Gong, F. Du, Z. H. Xia, M. Durstock and L. M. Dai, *Science*, 2009, **323**, 760–764.
10 Y. G. Li, W. Zhou, H. L. Wang, L. M. Xie, Y. Y. Liang, F. Wei, J. C. Idrobo, S. J. Pennycook and H. J. Dai, *Nat. Nanotechnol.*, 2012, **7**, 394–400.
11 J. Suntivich, H. A. Gasteiger, N. Yabuuchi, H. Nakanishi, J. B. Goodenough and Y. Shao-Horn, *Nat. Chem.*, 2011, **3**, 546–550.
12 S. H. Oh, R. Black, E. Pomerantseva, J. H. Lee and L. F. Nazar, *Nat. Chem.*, 2012, **4**, 1004–1010.
13 M. Lefevre, E. Proietti, F. Jaouen and J. P. Dodelet, *Science*, 2009, **324**, 71–74.
14 D. H. Deng, L. Yu, X. Q. Chen, G. X. Wang, L. Jin, X. L. Pan, J. Deng, G. Q. Sun and X. H. Bao, *Angew. Chem., Int. Ed.*, 2013, **52**, 371–375.
15 C. H. Cui, H. H. Li, J. W. Yu, M. R. Gao and S. H. Yu, *Angew. Chem., Int. Ed.*, 2010, **49**, 9149–9152.
16 A. Serov and C. Kwak, *Appl. Catal., B*, 2009, **90**, 313–320.
17 I. Kruusenberg, L. Matisen, Q. Shah, A. M. Kannan and K. Tammeveski, *Int. J. Hydrogen Energy*, 2012, **37**, 4406–4412.
18 Y. J. Wang, J. L. Qiao, R. Baker and J. J. Zhang, *Chem. Soc. Rev.*, 2013, **42**, 5768–5787.
19 N. J. Robertson, H. A. Kostalik, T. J. Clark, P. F. Mutolo, H. D. Abruna and G. W. Coates, *J. Am. Chem. Soc.*, 2010, **132**, 3400–3404.
20 A. E. S. Sleightholme, J. R. Varcoe and A. R. Kucernak, *Electrochem. Commun.*, 2008, **10**, 151–155.
21 J. S. Guo, A. Hsu, D. Chu and R. R. Chen, *J. Phys. Chem. C*, 2010, **114**, 4324–4330.
22 M. Chatenet, L. Genies-Bultel, M. Aurousseau, R. Durand and F. Andolfatto, *J. Appl. Electrochem.*, 2002, **32**, 1131–1140.
23 M. H. Seo, S. M. Choi, H. J. Kim and W. B. Kim, *Electrochem. Commun.*, 2011, **13**, 182–185.
24 L. Jiang, A. Hsu, D. Chu and R. Chen, *J. Electrochem. Soc.*, 2009, **156**, B370–B376.
25 Y. Lee, A. Loew and S. H. Sun, *Chem. Mater.*, 2010, **22**, 755–761.
26 H. J. Yin, H. J. Tang, D. Wang, Y. Gao and Z. Y. Tang, *ACS Nano*, 2012, **6**, 8288–8297.
27 K. Asazawa, T. Sakamoto, S. Yamaguchi, K. Yamada, H. Fujikawa, H. Tanaka and K. Oguro, *J. Electrochem. Soc.*, 2009, **156**, B509–B512.
28 H. Tanaka, K. Asazawa, T. Sakamoto, T. Kato, M. Kai, S. Yamaguchi, K. Yamada and H. Fujikawa, *ECS Trans.*, 2008, **16**, 459–464.
29 O. Savadogo, K. Lee, K. Oishi, S. Mitsushima, N. Kamiya and K. I. Ota, *Electrochem. Commun.*, 2004, **6**, 105–109.
30 M. H. Shao, K. Sasaki and R. R. Adzic, *J. Am. Chem. Soc.*, 2006, **128**, 3526–3527.
31 C. H. Cui and S. H. Yu, *Acc. Chem. Res.*, 2013, **46**, 1427–1437.
32 H. Yano, J. Inukai, H. Uchida, M. Watanabe, P. K. Babu, T. Kobayashi, J. H. Chung, E. Oldfield and A. Wieckowski, *Phys. Chem. Chem. Phys.*, 2006, **8**, 4932–4939.

33 K. Kinoshita, *J. Electrochem. Soc.*, 1990, **137**, 845–848.
34 B. Lim, M. J. Jiang, P. H. C. Camargo, E. C. Cho, J. Tao, X. M. Lu, Y. M. Zhu and Y. N. Xia, *Science*, 2009, **324**, 1302–1305.
35 Z. W. Chen, M. Waje, W. Z. Li and Y. S. Yan, *Angew. Chem., Int. Ed.*, 2007, **46**, 4060–4063.
36 L. Xiao, L. Zhuang, Y. Liu, J. T. Lu and H. D. Abruna, *J. Am. Chem. Soc.*, 2009, **131**, 602–608.
37 J. L. Zhang, M. B. Vukmirovic, Y. Xu, M. Mavrikakis and R. R. Adzic, *Angew. Chem., Int. Ed.*, 2005, **44**, 2132–2135.
38 J. L. Zhang, M. B. Vukmirovic, K. Sasaki, A. U. Nilekar, M. Mavrikakis and R. R. Adzic, *J. Am. Chem. Soc.*, 2005, **127**, 12480–12481.
39 J. Greeley, I. E. L. Stephens, A. S. Bondarenko, T. P. Johansson, H. A. Hansen, T. F. Jaramillo, J. Rossmeisl, I. Chorkendorff and J. K. Norskov, *Nat. Chem.*, 2009, **1**, 552–556.
40 Y. H. Bing, H. S. Liu, L. Zhang, D. Ghosh and J. J. Zhang, *Chem. Soc. Rev.Chem Soc Rev*, 2010, **39**, 2184–2202.
41 Y. Song, K. Liu and S. W. Chen, *Langmuir*, 2012, **28**, 17143–17152.
42 G. Q. He, Y. Song, B. Phebus, K. Liu, C. P. Deming, P. G. Hu and S. W. Chen, *Sci. Adv. Mater.*, 2013, **5**, 1727–1736.
43 K. Liu, Y. Song and S. W. Chen, *J. Power Sources*, 2014, **268**, 469–475.
44 K. Liu, X. W. Kang, Z. Y. Zhou, Y. Song, L. J. Lee, D. Tian and S. W. Chen, *J. Electroanal. Chem.*, 2013, **688**, 143–150.
45 Z. Y. Zhou, X. W. Kang, Y. Song and S. W. Chen, *Chem. Commun.*, 2012, **48**, 3391–3393.
46 F. Gloaguen, F. Andolfatto, R. Durand and P. Ozil, *J. Appl. Electrochem.*, 1994, **24**, 863–869.
47 N. M. Markovic, T. J. Schmidt, V. Stamenkovic and P. N. Ross, *Fuel Cells*, 2001, **1**, 105–116.
48 R. Y. Wang, C. X. Xu, X. X. Bi and Y. Ding, *Energy Environ. Sci.*, 2012, **5**, 5281–5286.
49 M. H. Shao, T. Yu, J. H. Odell, M. S. Jin and Y. N. Xia, *Chem. Commun.*, 2011, **47**, 6566–6568.
50 I. Spanos, C. P. Rellan, L. Altmann, M. Baumer and M. Arenz, *Int. J. Hydrogen Energy*, 2014, **39**, 9143–9148.
51 C. Wang, N. M. Markovic and V. R. Stamenkovic, *ACS Catal.*, 2012, **2**, 891–898.
52 Q. W. Tang, L. H. Jiang, J. Liu, S. L. Wang and G. Q. Sun, *ACS Catal.*, 2014, **4**, 457–463.
53 X. P. Sun, S. J. Dong and E. K. Wang, *Macromolecules*, 2004, **37**, 7105–7108.
54 X. C. Wang, J. C. Yu, C. M. Ho and A. C. Mak, *Chem. Commun.*, 2005, 2262–2264.
55 G. Johansson, J. Hedman, A. Berndtsson, M. Klasson and R. Nilsson, *J. Electron Spectrosc. Relat. Phenom.*, 1973, **2**, 295–317.
56 J. A. Creighton and D. G. Eadon, *J. Electron Spectrosc. Relat. Phenom.*, 1991, **87**, 3881–3891.
57 S. W. Hsu, K. On, B. Gao and A. R. Tao, *Langmuir*, 2011, **27**, 8494–8499.
58 S. Link, Z. L. Wang and M. A. El-Sayed, *J. Phys. Chem. B*, 1999, **103**, 3529–3533.
59 H. D. Kaesz and R. B. Saillant, *Chem. Rev.*, 1972, **72**, 231–281.
60 L. Andrews and X. F. Wang, *J. Am. Chem. Soc.*, 2003, **125**, 11751–11760.
61 W. Chen, N. B. Zuckerman, X. W. Kang, D. Ghosh, J. P. Konopelski and S. W. Chen, *J. Phys. Chem. C*, 2010, **114**, 18146–18152.
62 X. Kang, N. B. Zuckerman, J. P. Konopelski and S. Chen, *J. Am. Chem. Soc.*, 2012, **134**, 1412–1415.
63 G. Q. He, Y. Song, K. Liu, A. Walter, S. Chen and S. W. Chen, *ACS Catal.*, 2013, **3**, 831–838.
64 A. Schumpe, I. Adler and W. D. Deckwer, *Biotechnol. Bioeng.*, 1978, **20**, 145–150.
65 N. A. Anastasijevic, Z. M. Dimitrijevic and R. R. Adzic, *Electrochim. Acta*, 1986, **31**, 1125–1130.
66 N. M. Markovic, H. A. Gasteiger, B. N. Grgur and P. N. Ross, *J. Electroanal. Chem.*, 1999, **467**, 157–163.
67 P. Singh and D. A. Buttry, *J. Phys. Chem. C*, 2012, **116**, 10656–10663.
68 J. Zhang, *PEM fuel cell electrocatalysts and catalyst layers: fundamentals and applications*, Springer, London, 2008.
69 B. P. Vinayan, R. Nagar and S. Ramaprabhu, *J. Mater. Chem.*, 2012, **22**, 25325–25334.
70 P. Quaino, N. B. Luque, R. Nazmutdinov, E. Santos and W. Schmickler, *Angew. Chem., Int. Ed.*, 2012, **51**, 12997–13000.
71 Y. G. Suo, L. Zhuang and J. T. Lu, *Angew. Chem., Int. Ed.*, 2007, **46**, 2862–2864.
72 A. Q. Wang, J. H. Liu, S. D. Lin, T. S. Lin and C. Y. Mou, *J. Catal.*, 2005, **233**, 186–197.
73 A. B. Anderson, *Electrochim. Acta*, 2002, **47**, 3759–3763.
74 Y. H. Cheng, W. Y. Li, X. Z. Fan, J. G. Liu, W. G. Xu and C. W. Yan, *Electrochim. Acta*, 2013, **111**, 635–641.
75 C. L. Lai, P. Kolla, Y. Zhao, H. Fong and A. L. Smirnova, *Electrochim. Acta*, 2014, **130**, 431–438.
76 Y. L. Tsai, K. L. Huang, C. C. Yang, J. S. Ye, L. S. Pan and C. L. Lee, *Int. J. Hydrogen Energy*, 2014, **39**, 5528–5536.
77 D. A. Slanac, A. Lie, J. A. Paulson, K. J. Stevenson and K. P. Johnston, *J. Phys. Chem. C*, 2012, **116**, 11032–11039.
78 C. L. Lee, H. P. Chiou, K. C. Chang and C. H. Huang, *Int. J. Hydrogen Energy*, 2011, **36**, 2759–2764.
79 L. Jiang, A. Hsu, D. Chu and R. Chen, *Electrochim. Acta*, 2010, **55**, 4506–4511.
80 D. A. Slanac, W. G. Hardin, K. P. Johnston and K. J. Stevenson, *J. Am. Chem. Soc.*, 2012, **134**, 9812–9819.
81 C. L. Lee and C. C. Syu, *Int. J. Hydrogen Energy*, 2011, **36**, 15068–15074.

